PLATINUM-GROUP ELEMENTS-BEARING PYRITES FROM THE AGUABLANCA Ni-Cu SULPHIDE DEPOSIT (SW SPAIN): A LA-ICP-MS STUDY

RUBÉN PIÑA[1,*] et al.

[1] Departamento de Cristalografía y Mineralogía, Facultad de Ciencias Geológicas, Universidad Complutense de Madrid, c/ José Antonio Novais s/n, 28040 Madrid, Spain

Abstract: Despite the fact that pyrite is a relatively common phase in Ni-Cu-Platinum-Group Elements (PGE) magmatic sulphide deposits, it has been neglected in the studies on PGE distribution in favour of pyrrhotite, pentlandite and chalcopyrite. An example of this is the Aguablanca deposit, where although pyrite is an important phase in the semi-massive ore and an early study has revealed that it hosts traces of PGE, the presence and origin of PGE into the pyrite has not been investigated in detail. With this in mind, we have measured by laser ablation ICP-MS the content of these and other chalcophile elements (Au, Ag, Co, Ni, Cu, Se, Sb, As, Bi and Te) in pyrite exhibiting different textures. The results show that 1) large idiomorphic pyrite is compositionally-zoned with Os-Ir-Ru-Rh-As-rich layers and Se-Co-rich layers; 2) some idiomorphic pyrites contain unusually high PGE contents (up to 32 ppm Rh and 9 ppm Pt); 3) ribbon-like and small-grained pyrites host IPGE (*i.e.*, Iridium-group PGE, Os, Ir, Ru and Rh) in similar contents (100-200 ppb each) to the host pyrrhotite; and 4) pyrites replacing to plagioclase are depleted in most metals (*i.e*., PGE, Co, Ni and Ag). Overall, the different textural types of pyrite have similar abundances in Pd, Au, Se, Bi, Te, Sb and As. Mineralogical and compositional data suggests that pyrite is the result of the activity of late magmatic/hydrothermal fluids that triggered the partial replacement of pyrrhotite and plagioclase by pyrite, probably due to an increase in the sulphur fugacity during cooling. During this episode, pyrites inherited the IPGE content of mineral to that was replaced, whereas other elements such as Pd, Au and semi-metals were likely partially introduced into pyrite *via* altering fluids. These results highlight that pyrite can host appreciable amounts of PGE and therefore it should not be overlooked as a potential carrier of these metals in Ni-Cu-(PGE) sulphide deposits.

Key-words: sulphides, pyrite, platinum-group elements, LA-ICP-MS, Aguablanca.

1. Introduction

In the recent years, the development of microanalytical techniques such as laser ablation inductively coupled plasma mass spectrometry (LA-ICP-MS) has let to better understand the distribution of platinum-group elements (Os, Ir, Ru, Rh, Pt and Pd, PGE) in Ni-Cu-(PGE) ore deposits by measuring the *in situ* concentrations of these elements in sulphides (*i.e.*, pyrrhotite, pentlandite and chalcopyrite) (*e.g.*, Huminicki *et al.*, 2005; Barnes *et al.*, 2008; Godel *et al.*, 2007; Holwell & McDonald, 2007). These studies have highlighted the close relationship between PGE and sulphides, with IPGE (*i.e.*, Os, Ir, Ru and Rh) typically occurring in solid solution within pyrrhotite and pentlandite, and Pt and Pd usually as discrete platinum-group minerals (PGM, bismuthotellurides, tellurides, arsenides, and sulphides) associated with sulphides and some Pd within pentlandite. Pyrite is commonly present in minor amounts in magmatic sulphide deposits and is considered to form by either exsolution from S-rich monosulfide solid solution (mss) and by replacement of pyrrhotite by late magmatic/hydrothermal fluids (Farrow & Watkinson, 1992; Naldrett *et al.*, 1999). Although previous studies have revealed that pyrite can host some PGE (*e.g.*, Oberthür *et al.*, 1997; Gervilla & Kojonen, 2002), it has been neglected during laser ablation analyses of sulphides. However, recently a number of studies have reported variable amounts of PGE within pyrite (Lorand & Alard, 2011; Dare *et al.*, 2011; Djon & Barnes, 2012; Piña *et al.*, 2012; Knight *et al.*, 2012). Most of these authors found that pyrites with different textures contain distinct PGE and chalcophile element contents. In general, the pyrites that are rich in IPGE are associated with pyrrhotite and pentlandite and are thought to have formed either by exsolution from mss or by replacement of the mss component of the sulphides (pyrrhotite and pentlandite). In contrast, pyrites that are poor in IPGE are thought to have directly precipitated from hydrothermal or metamorphic fluids.

At the Aguablanca Ni-Cu sulphide deposit (SW Spain, Tornos *et al.*, 2006; Lunar *et al.*, 2008; Piña *et al.*, 2010), an early laser ablation study focused on the PGE distribution in the magmatic sulphides revealed that pyrite hosts traces of PGE (Piña *et al.*, 2012). Some large idiomorphic grains of pyrite contain high concentrations of Pt (up to 15 ppm) and Rh (4-31 ppm), and ribbon-like pyrite grains, apparently replacing to pyrrhotite, have Os, Ir, Ru and Rh in the order to ~ 30-360 ppb for each metal. Further study shows that there are more pyrite textural types and we have now determined by LA-ICP-MS the concentration of PGE and other chalcophile elements

(Au, Ag, Ni, Co, Cu, Se, As, Sb, Bi and Te) in the different types of pyrite identified in Aguablanca (Ortega *et al*., 2004): (i) large idiomorphic grains, (ii) ribbon-like grains, (iii) small single or aggregated crystals within pyrrhotite, and (iv) pyrite crystals replacing to plagioclase. In addition to a better understanding of the origin of PGE within pyrite and the role of pyrite as carrier of these metals, these results will be useful in discussing which processes were involved in the formation of pyrites (*i.e*., exsolution from mss versus replacement of sulphides).

2. The Aguablanca Ni-Cu sulphide deposit

The Aguablanca ore deposit comprises an economic Ni-Cu sulphide mineralization (6.5 Mt @ 0.6 % Ni and 0.4 % Cu) located in the northern part of the Aguablanca mafic intrusion, SW Spain (Fig. 1). This intrusion (341±1.5 Ma, U/Pb on magmatic zircons, Romeo *et al*., 2006) forms part of the Santa Olalla Igneous Complex, a calk-alkaline plutonic group situated in the southern limb of the Variscan Olivenza-Monesterio antiform within the Ossa-Morena Zone of the Iberian Massif. The Aguablanca intrusion was emplaced during the Variscan transpressive orogeny across a hundred-meter-scale, open tensional fracture developed under sinistral strike-slip ductile strain regime (Romeo *et al*., 2008). The sulphide mineralization occurs in form of a subvertical magmatic breccia (250-300 m wide N-S, up to 600 m long E-W and 600 m deep) hosted by cumulate-textured gabbronorites and norites. The breccia is made up of gabbronorite cumulates containing semi-massive and disseminated sulphides (hereafter semi-massive and disseminated ore, respectively) that host unmineralized mafic-ultramafic fragments coming from an unexposed mafic-ultramafic sequence situated below the Aguablanca intrusion (Piña *et al*., 2006). Small chalcopyrite veinlets are present cross-cutting the semi-massive and disseminated ores. Primary pyroxene and plagioclase of the host igneous rocks are variably altered to a secondary silicate assemblage comprising chlorite, actinolite, epidote, sericite and talc. The emplacement of the breccia probably took place when the mafic-ultramafic sequence was disrupted by the explosive injection of Ni-Cu sulphide-bearing gabbronorite melts due to the opening of tensional fractures related to the emplacement of the Aguablanca intrusion (Piña *et al*., 2010).

The ore mineralogy comprises pyrrhotite + pentlandite + chalcopyrite ± magnetite and pyrite. Pyrite and pentlandite are occasionally replaced to marcasite and violarite, respectively. The three ore types identified at Aguablanca, semi-massive,

disseminated and chalcopyrite-veined ores, show sulphide modal abundances and PGE patterns consistent with the fractionation of a sulphide melt (Piña *et al*., 2008, 2012). Thus, the semi-massive ore, formed mostly by pyrrhotite and pentlandite with minor chalcopyrite (Ni/Cu averages 7.3, Piña *et al*., 2008), represents a mss cumulate rich in Os-Ir-Ru-Rh and poor in Pd-Pt-Au-Cu, whereas the Cu-Pd-Au-(Pt)-rich chalcopyrite veinlets represent the crystallization of a residual Cu-rich sulphide liquid formed after mss crystallization. The disseminated ore, made up of pyrrhotite and roughly equal proportions of pentlandite and chalcopyrite (Ni/Cu averages 0.85, Piña *et al*., 2008), represents the *in situ* crystallization of an original sulphide melt. Ortega *et al*. (2004), Piña *et al*. (2008) and Suárez *et al*. (2010) have identified a similar PGM assemblage made up, in a decreasing order of abundance, of merenskyite ($PdTe_2$), palladian melonite ($NiTe_2$), michenerite (PdBiTe), moncheite ($PtTe_2$) and sperrylite ($PtAs_2$). These PGM are mostly included within sulphides, mainly pyrrhotite and pentlandite, and commonly exhibit rounded and lath morphologies. Os, Ir, Ru and Rh mostly occur in solid solution within pyrrhotite and pentlandite, ~ 30% of the bulk Pd is within pentlandite and Pt is not in any sulphide phase except for a few pyrite grains that host up to 15 ppm Pt (Piña *et al*., 2012). These results are interpreted to suggest that PGE and chalcophile elements were collected by a sulphide liquid and incorporated into the sulphide minerals. As the temperature fell, Pd and Pt exsolved along with Bi, Te and As form the observed PGM assemblage.

3. Textural types of pyrite

Pyrite is a relatively common sulphide phase in the semi-massive ore of Aguablanca Ni-Cu deposit. It can reach up to 10-15 modal % of the total sulphides in areas with strong microfracturing and intense retrograde alteration of primary silicates to secondary hydrous silicates. In contrast, its presence in the disseminated and chalcopyrite-veined ores is quite insignificant, being generally absent or in amounts lower than 1 modal %. Pyrite is typically associated with pyrrhotite. Four different textural types of pyrite have been recognized (Fig. 2): *a*) large idiomorphic-subidiomorphic crystals (1-5 mm in size) hosted by pyrrhotite (Fig. 2a-b); *b*) small subhedral single crystals or aggregates (up to 600 μm) within pyrrhotite in spatial association with pentlandite and chalcopyrite (hereafter named small-grained pyrites) (Fig. 2c-d); *c*) ribbon-like crystals (0.5-3 mm long) within pyrrhotite (Fig. 2e-f); and *d*) irregular crystals replacing partial to totally to

plagioclase (Fig. 2g-h). Typically, in samples where pyrite is present, all textural types are present although the modal proportions widely vary from one sample to another.

4. Analytical methods

Polished blocks were studied by optical microscope to select sites for laser ablation analyses in the different textural types of pyrite. The trace elements were determined at LabMaTer, Université du Quebec à Chicoutimi (UQAC), Canada, using laser ablation inductively coupled plasma mass spectrometry (LA-ICP-MS). The UQAC laser ablation system consists of an Agilent 7700x mass spectrometer with an Excimer 193nm Resonetics Resolution M-50 laser ablation probe. Two samples, reference materials and blanks were placed in the chamber together. The reference materials and blanks were run before and after the two samples and between them. The spectrum was collected for 30 sec with the laser switch off to determine the base line. Then, line scans across the pyrite grains were carried out using a beam of 55 µm, a laser frequency of 15 Hz, a power of 0.5mJ/cm^3 and a stage speed of 5 µm/s. An argon-helium gas mix was used as carrier gas. The material was then analysed using the mass spectrometer in time resolution mode using mass jumping and a dwell time of 10 msec/peak. The following isotopes were monitored: ^{29}Si, ^{33}S, ^{34}S, ^{53}Cr, ^{57}Fe, ^{59}Co, ^{60}Ni, ^{61}Ni, ^{63}Cu, ^{65}Cu, ^{66}Zn, ^{68}Zn, ^{75}As, ^{82}Se, ^{101}Ru, ^{103}Rh, ^{105}Pd, ^{107}Ag, ^{108}Pd, ^{111}Cd, ^{121}Sb, ^{125}Te, ^{189}Os, ^{193}Ir, ^{195}Pt, ^{197}Au and ^{209}Bi. Data reduction was carried out using Iolite software (Paton *et al.*, 2011). Internal standardization was based on ^{57}Fe using the mean iron values in each pyrite (taken from Table 1, Piña *et al.*, 2012). The certified reference material Laflamme Po727, which is a synthetic FeS doped with ~ 40 ppm of each PGE and Au (Table S1) provided by the Memorial University of Newfoundland was used to calibrate for PGE and Au. For the rest of elements, we used the certified reference material MASS-1, a ZnCuFeS pressed powder pellet provide by United State Geological Survey and doped with 50-70 ppm Ag, As, Co, Bi, Sb, Se and Te (Table S1). The calibrations were monitored using the in-house materials UQAC-MSS1 and JB-MSS5. The material JB-MSS5 is a synthetic FeS with 1 wt.% Ni, 20-65 ppm PGE and Au and 50-80 ppm As, Ag, Bi, Sb, Se and Te (Table S1) provided by Prof. Brenan of the University of Toronto. The material UQAC-MSS1 consists of a synthetic $NiFeS_2$ provided by A. Peregoedova doped with ~2 ppm PGE and Au, 0.3-0.1 ppm Ag, Sb, Te and Bi, 5 ppm Se and ~ 70 ppm Co (Table S1). ^{101}Ru was corrected for ^{61}Ni interference by using

UQAC-MSS1. ^{103}Rh and ^{105}Pd were corrected for $^{63}Cu^{40}Ar$ and $^{65}Cu^{40}Ar$, respectively, by running a $(CuFe)S_2$ blank at the beginning and end of each session. The pyrite contains very little Cu thus the Cu correction on Rh and Pd is less than detection levels for these elements. Detection limits for laser analyses were calculated using 3 sigma of the background for the gas blank for each pyrite analyses. Tables with individual analyses for pyrite are listed in Table S2 and a summary with the concentrations is reported in Table 1. In those cases where the ICP-MS signal revealed variations in the content of some elements from rim to core (reflecting a possible zoning), maps of the element distribution were made. For mappings, a beam size of 25 μm, a laser frequency of 15 Hz, a power of 5 mJ/pulse and a speed of laser displacement of 20 μm/s were used. It took between 2 to 4 hours to map each grain. The maps show the relative concentration of the element and are semi-quantitative. With the proposal of comparing the trace element concentrations between pyrite and host pyrrhotite, we also analyzed pyrrhotite grains of the same samples (summary in Table 1 and whole analyses in Table S3). The obtained concentrations are in agreement with those already published by Piña *et al*. (2012).

5. Laser ablation results

5.1 Large idiomorphic pyrite

These pyrites are characterized by displaying systematic variations in PGE content from rim to core (Fig. 3a). Arsenic, Os, Ir, Ru and Rh are spatially associated each other, occurring as enriched bands or layers that generally surround the core of the crystals (Fig. 4a-b). These IPGE-As-rich zones coincide with minimum values in Se and Co, both of which reach maximum values at the rims of the crystals. The zoning of the pyrite in Figure 4b differs somewhat from that of most zoned pyrites. As in those, it displays Co-rich rims and Os-Ir-Ru-Rh-As-rich concentric layers oriented in parallel to the grain boundaries. However, this pyrite exhibits bands enriched in Pt which surprisingly do not coincide with those enriched in IPGE and As, but rather coincides with high Co values. This pyrite represents an unusual case because most of pyrites are unzoned relative to Pt, with values typically lower to 0.3 ppm. Although highly variable, PGE-zoned pyrites typically contain more than 1 ppm in Os, Ir, Ru and Rh, with values up to 2.8 ppm Os, 6.6 ppm Ir, 7.1 ppm Ru, and 32 ppm Rh. Other elements

such as Bi, Te, Sb, Pd, and Au do not show any zoning, occurring with relatively constant concentrations throughout the crystals (Fig. 3b).

5.2 Ribbon-like pyrite

Individual grains of this type of pyrite are compositionally homogeneous with no appreciable variation in the abundance of trace elements, including PGE, from core to rim (Fig. 3c-d). The ICP-MS signal is flat and stable, indicating that these elements are really in solid solution within pyrite. Osmium, Ir, Ru and Rh are present at around 100 ppb each, Pt is typically below the detection limit (~ 7 ppb) and Au and Pd average 239 and 75 ppb, respectively (Table 1). Nickel and Co contents range 4036-62000 ppm Ni and 1839-8140 ppm Co, similar values to those measured by Ortega *et al*. (2004) using electron microprobe. Selenium averages 98.4 ± 12.3 ppm, Te and Sb typically range 1-10 ppm, and As and Bi contents are variable, ranging 5-4100 ppm and 2.3-62.2 ppm, respectively. Silver is also variable, 6-25.6 ppm. The shape of the primitive mantle-normalized trace element patterns are very similar to those of the host pyrrhotite (Fig. 5), with Os, Ir, Ru, Rh and Se occurring in similar concentrations, but Ni, Co, Pd, Au, Ag, As, Sb, Te and Bi being higher in pyrite.

5.3 Small-grained pyrite

The primitive mantle-normalized trace element profile of this type of pyrites is almost identical to that of ribbon-like pyrite (Fig. 5). In general, small-grained pyrites contain slightly more Os, Ir, Ru and Rh: 130 ± 30 ppb Os, 247 ± 47 ppb Ir, 207 ± 35 ppb Ru and 190 ± 32 ppb Rh. Platinum is invariably below the detection limit, Pd ranges 13-161 ppb and Au, 18-185 ppb (typically < 60 ppb). Nickel is also slightly higher (6490-46000 ppm), but Co and Se range in similar values, 1393-9170 ppm Co and 80-106 ppm Se. Antimony, Bi and Te are commonly below 5 ppm and Ag averages 7.3 ppm with values up to 27.4 ppm. As in the case of the ribbon-like pyrite, the normalized values of Os, Ir, Ru and Rh are very similar to those of the host pyrrhotite, whereas the rest of trace elements are preferentially concentrated in the pyrite (Fig. 5).

5.4 Pyrite replacing plagioclase

PGE, Co, Ni and Ag contents in this type of pyrite are notably lower than in the pyrites associated with sulphides (Fig. 5). Osmium, Ir, Ru and Pt occur typically below the detection limit (20, 4, 6 and 7 ppb, respectively), and Rh and Pd are in concentrations

lower to 30 and 170 ppb, respectively. Gold contents range from 12 to 370 ppb and Ag ranges from 0.25 to 2.11 ppm. Nickel and Co contents are lower to 2740 and 126 ppm, respectively. Selenium (94.8 ± 39.8 ppm), Te (1.7 ± 0.9 ppm), Sb (3.6 ± 2.6 ppm), As (593 ± 647 ppm) and Bi (1.8 ± 2.1 ppm) contents are quite similar to the other textural types of pyrite.

6. Discussion

6.1 Origin of pyrite

The sulphide assemblage, pyrrhotite + pentlandite ± chalcopyrite, of the Aguablanca semi-massive ore represents a typical example of Fe-rich monosulphide solid solution (mss) cumulate with minor amounts of Cu-rich sulphide liquid, formed by the fractionation and crystallization of an immiscible sulphide melt (Ortega *et al*., 2004; Piña *et al*., 2008, 2012). Once crystallized, mss started to decompose, forming pyrrhotite and pentlandite below 650ºC, whereas chalcopyrite exsolved from intermediate solid solution (iss) previously formed from the Cu-rich sulphide liquid trapped among the mss grains. The origin of pyrite is much more uncertain. Two possible origins are commonly attributed for pyrite in magmatic sulphide assemblages: exsolution from S-rich mss on cooling (Naldrett *et al*., 1967), or replacement of pre-existing sulphides, mostly pyrrhotite and chalcopyrite, by late magmatic/hydrothermal fluids (*e.g.*, Naldrett *et al*., 1999; Dare *et al*., 2011; Su & Lesher, 2012). Experimental studies have shown that pyrite can exsolve from mss at temperatures below 700ºC if the mss composition falls on its S-rich side of the Fe-Ni-S ternary diagram (Naldrett & Kullerud, 1967; Naldrett *et al*., 1967). In contrast, if mss composition falls on its S-poor side, pentlandite will be the exsolving phase from mss and pyrite will not form. According to these experimental studies, pyrite and pentlandite cannot co-exist together until 230ºC when the mss tie line separating pyrite and pentlandite of the Fe-Ni-S diagram breaks. Therefore, if pyrite is an early exsolution phase, pentlandite can only form at temperatures below ~ 230ºC. This situation seems unlikely to exist in the semi-massive ore of Aguablanca because a number of evidence suggests that pentlandite started to exsolve from mss at temperatures close to 610ºC (its thermal maximum): the coarse-grained nature of pentlandite, its abundance and high Pd contents (~ 2 ppm, Piña *et al*., 2012). High contents of Pd in pentlandite are attributed to Pd diffusion into pentlandite from iss and mss during its exsolution (Barnes *et al*., 2006; Dare *et al*.,

2011; Piña *et al*., 2012). This diffusion process is efficient at high temperatures and is unlikely to exist at temperatures as low as 230ºC as is further indicated by the Pd-depleted nature of pentlandite flames (< 0.15 ppm, Piña *et al*., 2012) formed by exsolution from mss at temperatures below 250ºC (Kelly & Vaughan, 1983). Alternatively, pyrite could form below 230ºC, however the presence of significant amounts of IPGE in the pyrite provides evidence that it had to form at high temperatures as well (*e.g.*, Dare *et al*., 2011).

The pyrite that replaces to plagioclase is clearly the result of the activity of late magmatic/hydrothermal fluids, and hence can provide further evidence on the origin of the sulphide-hosted pyrites. The shape of the mantle-normalized profiles of trace elements in this pyrite is very similar to the profile of the pyrites texturally related to sulphides (Fig. 5). With the exception of IPGE and other metals such as Ni, Co or Ag, all pyrite types share similar concentrations in other trace elements such as Bi, Te, Sb, Se and As. This similarity is even more significant considering the S/Se ratio. S/Se ratio of pyrite replacing plagioclase averages 6071 ± 1841, whereas that of ribbon-like and small-grained pyrites is 5365 ± 720 and 5552 ± 591, respectively. If pyrites associated with sulphides are primary in origin (*i.e.*, exsolution from mss) and those related to plagioclase are secondary, the contents and distribution patterns of trace elements should be quite different and this is not the case at all. Thus, we suggest that all pyrite types, despite their textural variety, are genetically linked and related to the circulation of late magmatic/hydrothermal fluids that caused the replacement of pyrrhotite and plagioclase by pyrite. A similar formation mechanism has been also proposed for pyrite in some of the Sudbury and Lac des Iles deposits in Canada (Dare *et al*., 2011; Djon & Barnes, 2011) and in Wengeqi in China (Su & Lesher, 2012). The textural variety of pyrites in Aguablanca can be due to internal characteristics of host pyrrhotite. Thus, the ribbon-like pyrites can be the result of preferential nucleation and growth of pyrite on pre-existing twin planes of pyrrhotite (Ortega *et al*., 2004). Lorena?

The hydration of igneous silicates to form secondary hydrous silicates such as chlorite, actinolite and epidote in greenschist alteration facies decreases H_2O and increases S and fS_2 of the system (*e.g.*, Kanitpanyacharoen & Boudreau, 2012). The fS_2 increase of the fluids can drive the stabilization of pyrite over pyrrhotite in the logfS_2-T binary diagram (Fig. 6). The host igneous rocks in Aguablanca underwent a locally very intense retrograde alteration with clinopyroxene being replaced by actinolite and chlorite, orthopyroxene by actinolite and talc, and plagioclase by sericite, epidote, chlorite and

carbonates. The most intensively altered rocks often occur associated with areas of strong microfracturing and a relatively high amount of pyrite. We suggest that this subsolidus alteration event, driven by low-temperature hydrothermal fluids (~ 350ºC), caused an increase of fS_2 leading to the formation of the different types of pyrite.

6.2 Platinum-group and chalcophile elements into pyrite

One of the most interesting and striking features found in this study is the zoned distribution displayed by PGE in the idiomorphic pyrite. Compositionally zoned pyrites with respect to elements as Ni, Co or As are reported in the literature (*e.g.*, Craig & Solberg, 1999; Pal *et al*., 2009; Thomas *et al*., 2011), but pyrites exhibiting zoning with respect to PGE are scarcely documented. Recently, Hanley *et al*. (2010) reported Pt, Pd, Co and Ni zoning in pyrites from alkaline Cu-Au porphyries of the Canadian Cordillera and Dare *et al*. (2011) described pyrites showing oscillatory zoning with respect to Co, IPGE, As, Ni and Se in pyrrhotite-rich samples from the McCreedy East deposit in Sudbury, Canada. The zoning of these pyrites is very similar to the zoning observed in Aguablanca: IPGE (*i.e.*, Os, Ir, Ru and Rh) and As are closely associated each other in layers parallel to the grain boundaries and Se and Co are concentrated in relatively depleted in PGE and As layers. Dare *et al*. (2011) proposed that this zoning can be the result of "boundary layer effect" during the growth of pyrite from mss. At the beginning of pyrite growth, IPGE and As are preferentially incorporated into pyrite leaving the mss at the pyrite-mss boundary relatively depleted in these elements. Because the growth of pyrite was probably faster than the diffusion of PGE, the next layer of pyrite to grow formed from PGE-depleted mss and incorporated Co and Se instead of PGE and As, respectively. Eventually the pyrite grew into an undepleted mss and was able to incorporate again the PGE and As, giving rise to a new layer enriched in these elements. The strong affinity shown by PGE for As (*e.g.*, Tomkins, 2010; Hanley, 2010; Godel *et al*., 2012; Piña *et al*., 2012) would satisfactorily explain the close relationship between them, with IPGE having somewhat higher preference to form bonds with As than bonds with S in the pyrite structure. According to Dare *et al*. (2011)'s model, the content of S of the mss would have been locally sufficiently high to exsolve pyrite at high temperature at the same time that in other parts the mss with lower S contents exsolved pentlandite. A similar mechanism, although considering pyrite growth by fluids from a previous pyrrhotite instead of exsolution from mss, could be invoked to explain the zoning observed in Aguablanca. The incorporation of As (probably sourced by the

fluids) substituting for S would be linked with the entry of IPGE residing into pyrrhotite for Fe^{2+}. According to zoning (Fig. 4), IPGE competed with Co for the sites occupied for Fe^{2+} whereas Se competed with As for the sites occupied for S^{2-}. This process would fail to explain the distribution of Pt in the pyrite mapped in the Figure 4b. Pyrrhotite and pentlandite in Aguablanca are strongly depleted in Pt, in agreement with the strong incompatible behavior of Pt into mss ($D_{Pt}^{mss/sulf}$ = 0.05-0.23, Li *et al.*, 1996) hence it is difficult to envisage Pt diffusion from these phases to pyrite. Alternatively, Djon & Barnes (2012) have suggested for Pt-rich pyrites from Lac des Iles, Canada, that pyrite incorporated Pt via reaction of hydrothermal fluids with $PtAs_2$ during the replacement of pyrrhotite and pentlandite. A similar hypothesis might be postulated in Aguablanca. Pyrrhotite and pentlandite host Pt-bearing PGM, mainly sperrylite $PtAs_2$ and moncheite $PtTe_2$ (Fig. 8 in Piña *et al.*, 2008) and partial dissolution of these phases by hydrothermal fluids has been proposed to explain irregular edges of sperrylite at the contact with secondary chlorite and the presence of moncheite into actinolite (Piña *et al.*, 2008). We suggest that in those cases where pyrrhotite hosted Pt-bearing phases, the fluids responsible of pyrrhotite replacement by pyrite probably dissolved these phases, being Pt available for introducing into pyrite. Surprisingly, Pt is negatively correlated with IPGE (Fig. 3a and 4b), thus it seems that Pt competed with Os, Ir, Ru and Rh for the sites occupied for Fe^{2+}.

The trace element content of the different types of pyrite can be explained by a combination of two factors: 1.- the abundance of trace elements in the minerals to what replace and 2.- the mobile/immobile behaviour of the elements during the circulation of fluids responsible of replacement of pyrrhotite and plagioclase by pyrite. Because plagioclase is not a carrier of PGE and Os, Ir, Ru and Rh are typically highly immobile elements (reference), pyrite replacing plagioclase is strongly depleted in these elements (Fig. 7). In contrast, ribbon-like pyrites and small-grained pyrites concentrate Os, Ir, Ru and Rh in almost identical amounts to those of host pyrrhotite (Fig. 5 and 7), suggesting that these pyrites inherited these elements from pyrrhotite. The situation is similar in the case of Ni and Co. These elements are also strongly depleted in pyrite replacing plagioclase suggesting that they were not mobilized, but their higher contents in the small-grained and ribbon-like pyrites in comparison to pyrrhotite (Fig. 7) suggests that some of these elements were likely diffused from pentlandite as well. Platinum is not present either pyrrhotite or plagioclase therefore most pyrites do not contain Pt. The content of Pd and Au in pyrites replacing pyrrhotite (~ 0.07 ppm Pd and 0.15 ppm Au,

Table 1) cannot be simply explained by an inheritance from the host pyrrhotite. Pyrrhotite does not host any of these elements whereas pentlandite only accounts for about 30% of the total bulk Pd (Piña *et al*., 2012). Like Ni and Co, some of Pd could diffuse from pentlandite, implying Pd mobility beyond the mutual grain boundary, but in the case of Au, this diffusion is unlikely because Au is not present in any primary sulphide. Pyrite replacing plagioclase contains Au in similar values to those of pyrite replacing pyrrhotite (Fig. 7), suggesting that Au behaved as a mobile element and incorporated into pyrites via fluids. According to Piña *et al*. (2008), the postmagmatic history in Aguablanca included the partial remobilization of Pd, Au and Cu by late magmatic/hydrothermal fluids after the sulphide crystallization. Indeed, these metals are highly mobile elements under certain conditions (*e.g.*, Gammons, 1996; Gammons & Williams-Jones, 1997) and their occurrence in pyrite replacing plagioclase indicates that they were really mobilized by fluids and later incorporated in similar proportions into the different types of pyrite. With regards to semimetals, except Se that it is roughly evenly distributed between pyrite and pyrrhotite, the rest of semimetals (*i.e*., As, Sb, Te and Bi) are significantly enriched in pyrites relative to pyrrhotite with quite similar proportions in all textural types (Fig. 7). All these elements were likely incorporated into pyrites via fluids but the relatively high contents of As and Sb in pyrites replacing plagioclase in comparison to those of Te and Bi seems to indicate that As and Sb were ultimately more strongly mobilized.

7. Conclusions remarks

The different textural types of pyrite present in Aguablanca are genetically related to the circulation of late magmatic/hydrothermal fluids during the subsolidus evolution of the ore that triggered the replacement of pyrrhotite and plagioclase by pyrite. These pyrite have significant contents of PGE and other chalcophile elements that are the result of complete

., interpreted as having formed by Basically, the content of these elements in, depends on the content of trace elements in the minerals to what pyrite replaces and mobility of these elements during the circulation of the fluids. This investigation has revealed that pyrites coexisting with the typical magmatic sulphide assemblage of Ni-Cu ores

(pyrrhotite + pentlandite + chalcopyrite) can host significant amounts of PGE and other chalcophile elements.

along with The different textural types of pyrite presents in Ni-Cu sulphide ore of Aguablanca are genetically related to, which triggered the These pyrites host distinct contents in PGE and other chalcophile elements as a function of the content of these elements in the mineral to what replace and the

Acknowledgements: The authors are grateful to Río Narcea Recursos S.A. for providing samples for this research. We would like to thank Dany Savard for his assistance with the laser ablation analyses. This research was financed by the Spanish research project CGL2007-60266 and the Canada Research Chair in Magmatic Metallogeny. Rubén Piña's visit at UQAC was funded with a "José Castillejo" travel aid financed by Spanish Ministry of Science.

References

Barnes, S.-J., Cox, R.A., Zientek, M.L. (2006): Platinum-group element, Gold, Silver and Base Metal distribution in compositionally zoned sulfide droplets from the Medvezky Creek Mine, Noril'sk, Russia. *Contrib. Mineral. Petrol*., **152**, 187-200.

Dare, S.A.S., Barnes, S.-J., Prichard, H.M., Fisher, P. C. (2011): Chalcophile and platinum-group element (PGE) concentrations in the sulfide minerals from the McCreedy East deposit, Sudbury, Canada, and the origin of PGE in pyrite. *Mineral. Deposita*., **46**, 381-407.

Djon, M.L.N. & Barnes, S.-J. (2012): Changes in sulfides and platinum-group minerals with the degree of alteration in the Roby, Twilight, and High Grade Zones of the Lac des Iles Complex, Ontario, Canada. *Mineral. Deposita*., on line first.

Farrow C.E.G. & Watkinson D.H. (1997): Diversity of precious-metal mineralization in footwall Cu-Ni-PGE deposits, Sudbury, Ontario: implications for hydrothermal models of formation. *Can. Mineral*, **35**, 817-839.

Gervilla, F. & Kojonen, K. (2002): The platinum-group minerals in the upper section of the Keivitsansarvi Ni-Cu-PGE deposit, northern Finland. *Can. Mineral*., **40**, 377-394.

Godel, B., Barnes, S.-J., Maier, W.D. (2007): Platinum-group elements in sulphide minerals, platinum-group minerals, and whole-rocks of the Merensky Reef (Bushveld Complex, South Africa): implications for the formation of the Reef. *J. Petrol*., **48**, 1569-1604.

Godel, B., González-Alvarez, I., Barnes, S. J., Barnes, S.-J., Parker, P. Day, J. (2012): Sulfide and sulfarsenides from the Rosie Nickel Prospect, Duketon Greenstone Belt, Western Australia. *Econ. Geol*., **107**, 275-294.

Hanley, J.J. (2007): The role of arsenic-rich melts and mineral phases in the development of high-grade Pt-Pd mineralization within komatiite-associated magmatic Ni-Cu sulfide horizons at Dundonald Beach South, Abitibi subprovince, Ontario, Canada. *Econ. Geol*., **102**, 305-317.

Hanley, J. J., MacKenzie, M. K., Warren, M. R., Guillong, M. (2010): Distribution and origin of platinum-group elements in alkalic porphyry Cu–Au and low sulfidation epithermal au deposits in the Canadian Cordillera. In: 11th international platinum symposium, program abstracts, Ontario Geological Survey, miscellaneous release-data 269

Holwell, D.A. & McDonald, I. (2007): Distribution of platinum-group elements in the Platreef at Overysel, northern Bushveld Complex: a combined PGM and LA-ICP-MS study. *Contrib. Mineral. Petrol*., **154**, 171-190.

Huminicki, M.A.E., Sylvester, P.J., Cabri, L.J., Lesher, C.M., Tubrett, M. (2005): Quantitative mass balance of platinum group elements in the Kelly Lake Ni-Cu-PGE deposit, Copper Cliff Offset, Sudbury. *Econ. Geol*., **100**, 1631-1646.

Hutchinson D. & McDonald, I. (2008): Laser ablation ICP-MS study of platinum-group elements in sulphides from the Platreef at Turfspruit, northern limb of the Bushveld Complex, South Africa. *Mineral. Deposita*., **43**, 695-711.

Kanitpanyacharoen, W. & Boudreau, A. E. (2012): sulfide-associated mineral assemblages in the Bushveld Complex, South Africa: platinum-group element enrichment by vapor refining by chloride-carbonate fluids. *Mineral. Deposita*., online.

Kelly, D.P., Vaughan, D.J., 1983. Pyrrhotine-pentlandite ore textures: a mechanistic approach. Mineral Mag. 47, 453-463.

Knight, R. D., Prichard, H. M., McDonald, I., Ferreira Filho, C. F. (2012): PGE mineralization in the Fazenda Mirabela intrusion, Bahia State, Brazil: distribution of PGE in base metal sulphides and PGM. 12th Nickel Symposium.

Li, C., Barnes, S.-J., Makovicky, E., Rose-Hansen, J. Makovicky, M. (1996): Partitioning of Ni, Cu, Ir, Rh, Pt and Pd between monosulfide solid solution and sulfide liquid: effects of composition and temperature. *Geochim. Cosmochim. Acta.*, **60**, 1231-1238.

Lorand, J.P. & Alard, O. (2011): Pyrite tracks assimilation of crustal sulfur in Pyrenean peridotites. *Miner. Petrol.*, **101**, 115-128..

Lunar, R.; Romeo, I.; Piña, R.; Capote, R.; Ortega, L.; Gervilla, F.; Quesada, C., Tejero, R. (2008): El yacimiento de Ni-Cu-(EGP) de Aguablanca (Macizo Ibérico): Marco tectónico, mineralogía, geoquímica, geocronología y modelo metalogenético. Instituto Geológico y Minero de España, Serie de Recursos Minerales, Madrid, 252 p.

McDonough, W.F. & Sun, S.-S. (1995): The composition of the Earth. *Chem. Geol.*, **120**, 223-253.

Naldrett, A.J. & Kullerud, G. (1967): A study of the Strathcona mine and its bearing on the origin of the nickel–copper ores of the Sudbury District, Ontario. *J. Petrol.*, **8**, 453–531.

Naldrett, A. J., Craig, J. R., Kullerud, G. (1967): The central portion of the Fe-Ni-S system and its bearing on pentlandite solution in iron-nickel sulfide ores. *Econ. Geol.*, **62**, 826-847.

Naldrett A.J., Asif M., Schandl E., Searcy T., Morrison G.G., Binney W.P., Moore C. (1999): Platinum group elements in the Sudbury ores: significance with respect to the origin of different ore zones and to the exploration for footwall ores. *Econ. Geol.*, **94**, 185–210.

Oberthür, T., Cabri, L.J., Weiser, T.W., McMahon, G., Müller, P. (1997): Pt, Pd and other trace elements in sulfides of the main sulfide zone, Great Dyke, Zimbabwe: a reconnaissance study. *Can. Mineral.*, **35**, 597-609.

Ortega, L., Lunar, R., García-Palomero, F., Moreno, T., Martín Estévez, J.R., Prichard, H.M., Fisher, P.C. (2004): The Aguablanca Ni-Cu-PGE deposit, southwestern Iberia: Magmatic ore-forming processes and retrograde evolution. *Can. Mineral.*, **42**, 325–335.

Paton, C., Hellstrom, J., Paul, B., Woodhead, J., Hergt, J. (2011): Iolite: freeware for the visualization and processing of mass spectrometric data. *J. Anal. At. Spectrom.*, **26**, 2508-2518..

Piña, R., Lunar, R., Ortega, L., Gervilla, F., Alapieti, T., Martínez, C. (2006): Petrology and geochemistry of mafic-ultramafic fragments from the Aguablanca (SW Spain) Ni-Cu ore breccia: Implications for the genesis of the deposit. *Econ. Geol.*, **101**, 865–881.

Piña, R., Gervilla, F., Ortega, L., Lunar, R. (2008): Mineralogy and geochemistry of platinum-group elements in the Aguablanca Ni-Cu deposit (SW Spain). *Mineral. Petrol.*, **92**, 259–282.

Piña, R., Romeo, I., Ortega, L., Lunar, R., Capote, R., Gervilla, F, Tejero, R., Quesada, C. (2010): Origin and emplacement of the Aguablanca magmatic Ni-Cu-(PGE) sulfide deposit, SW Iberia: a multidisciplinary research. *Geol. Soc. Amer. Bull.*, **122**, 915-925.

Piña, R., Gervilla, F., Barnes, S.-J., Ortega, L., Lunar, R. (2012): Distribution of platinum-group and chalcophile elements in the Aguablanca Ni-Cu sulfide deposit (SW Spain): evidence from a LA-ICP-MS study. *Chem. Geol.*, **302-303**, 61-75.

Piña, R., Gervilla, F., Barnes, S.-J., Ortega, L., Lunar, R. (2012): Partition coefficients of platinum-group and chalcophile elements between arsenide and sulfide phases as determined in the Beni Bousera Cr-Ni mineralization. *Econ. Geol.*, accepted.

Romeo, I., Lunar, R., Capote, R., Quesada, C., Dunning, G.R., Piña, R., Ortega, L. (2006): U/Pb age constraints on Variscan Magmatism and Ni-Cu-PGE metallogeny in the Ossa-Morena zone (SW Iberia). *J. Geol. Soc. London.*, **163**, 837–846.

Romeo, I., Tejero, R., Capote, R., Lunar, R. (2008): 3D gravity modelling of the Aguablanca Stock, tectonic control and emplacement of a Variscan gabbronorite bearing a Ni-Cu-PGE ore, SW Iberia. *Geol. Mag.*, **145**, 345–359.

Su, S. & Lesher, C. M. (2012): Genesis of PGE mineralization in the Wengeqi mafic-ultramafic complex, Guyang County, Inner Mongolia, China. *Mineral. Dep*., **47**, 197-207.

Suárez, S., Prichard, H.M., Velasco, F., Fisher, P.C., McDonald, I. (2010): Alteration of platinum-group minerals and dispersion of platinum-group elements during progressive weathering of the Aguablanca Ni-Cu deposit, SW Spain. *Mineral. Deposita*., **45**, 331-350.

Tomkins, A.G. (2010) Wetting facilitates late-stage segregation of precious metal-enriched sulfosalt melt in magmatic sulfide systems. *Geology*, **38**, 951-954.

Tornos, F., Galindo, C., Casquet, C., Rodríguez-Pevida, L., Martínez, C., Martínez, E., Velasco, F., Iriondo, A. (2006): The Aguablanca Ni-(Cu) sulfide deposit, SW Spain: geologic and geochemical controls and the relationship with a midcrustal layered mafic complex. *Mineral. Deposita*., **41**, 737–769.

Wilson, S.A., Ridley, W. I., Koenig, A. E. (2002): Development of sulfide calibration standards for laser ablation inductively-coupled mass spectrometry technique. *J. Anal. At. Spectrom*., **17**, 406-409.

Figure captions

Fig. 1. Location in the Iberian Massif and simplified geological map of Aguablanca mafic intrusion showing the location of the Ni-Cu ore. Modified from Piña *et al*. (2012).

Fig. 2. Photographs of reflected-light optical microscope showing the different textural types of pyrite recognized in semi-massive ore samples from the Aguablanca Ni-Cu sulphide deposit; Py, pyrite; Po, pyrrhotite; Pn, pentlandite; Ccp, chalcopyrite; Sil, silicate; Plag, plagioclase. (a-b) Large idiomorphic pyrites. (c-d) Small-grained pyrite texturally related to pentlandite and chalcopyrite. (e-f) Ribbon-like pyrites. (g-h) Pyrites replacing to plagioclase. Observe an idiomorphic pyrite grain within pyrrhotite in h.

Fig. 3. Spectra of trace element abundances obtained by LA-ICP-MS in idiomorphic (a-b) and ribbon-like (c-d) pyrite.

Fig. 4. Compositional zoning of large idiomorphic pyrites in semi-massive ore samples from the Aguablanca deposit. In b, the pyrite is also zoned with respect to Pt, opposite to most zoned pyrites.

Fig. 5. Primitive mantle-normalized trace element average profiles as determined by LA-ICP-MS for the different types of pyrite and host pyrrhotite. Primitive mantle values

are from McDonough & Sun (1995). When data are below the detection limit, these values were employed.

Fig. 6. Fe-S-O system as a function of temperature (ºC) and fS_2 (fO_2 is defined for QFM buffer). See text for additional discussion.

Fig. 7. Histogram showing the average content of trace elements in the different pyrite types divided by the average of pyrrhotite. When data are below the detection limit, these values were employed.

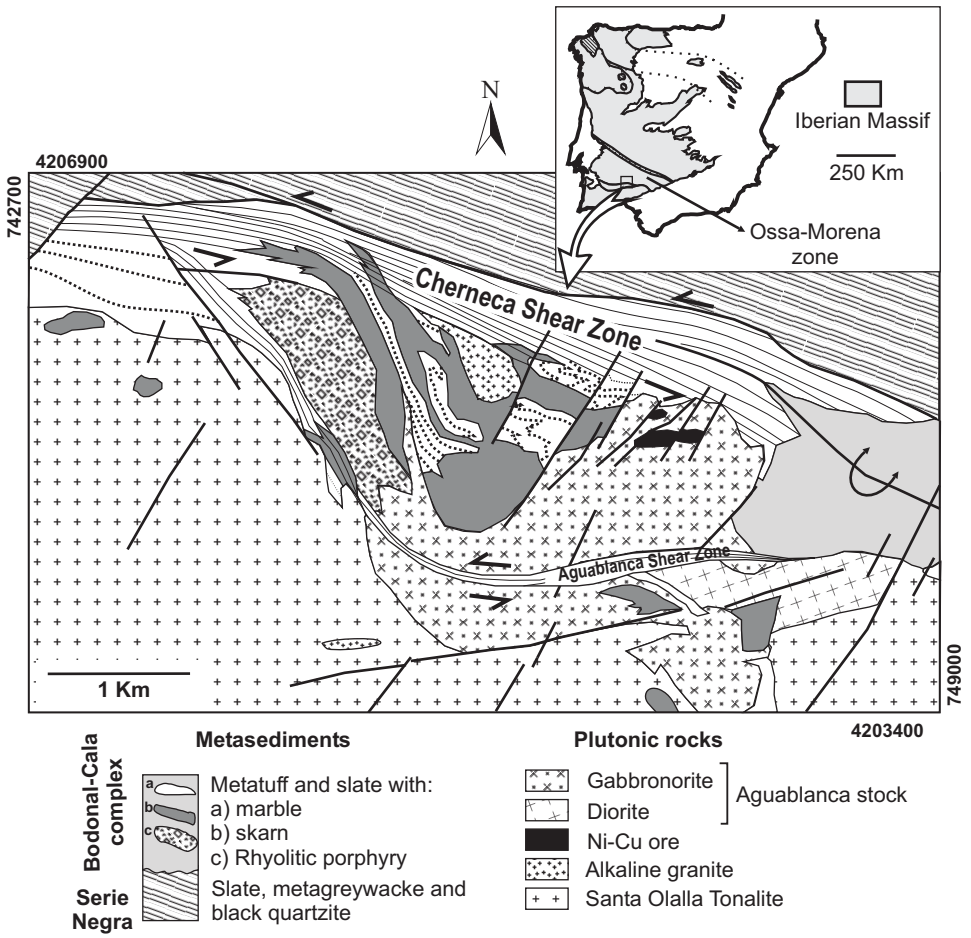
N
Iberian Massif
250 Km
Ossa-Morena zone
4206900
742700
Cherneca Shear Zone
Aguablanca Shear Zone
1 Km
749000
4203400
Metasediments
Plutonic rocks
Bodonal-Cala complex
a
b
c
Metatuff and slate with:
a) marble
b) skarn
c) Rhyolitic porphyry
Serie Negra
Slate, metagreywacke and black quartzite
Gabbronorite
Diorite
Aguablanca stock
Ni-Cu ore
Alkaline granite
Santa Olalla Tonalite

Figure 1

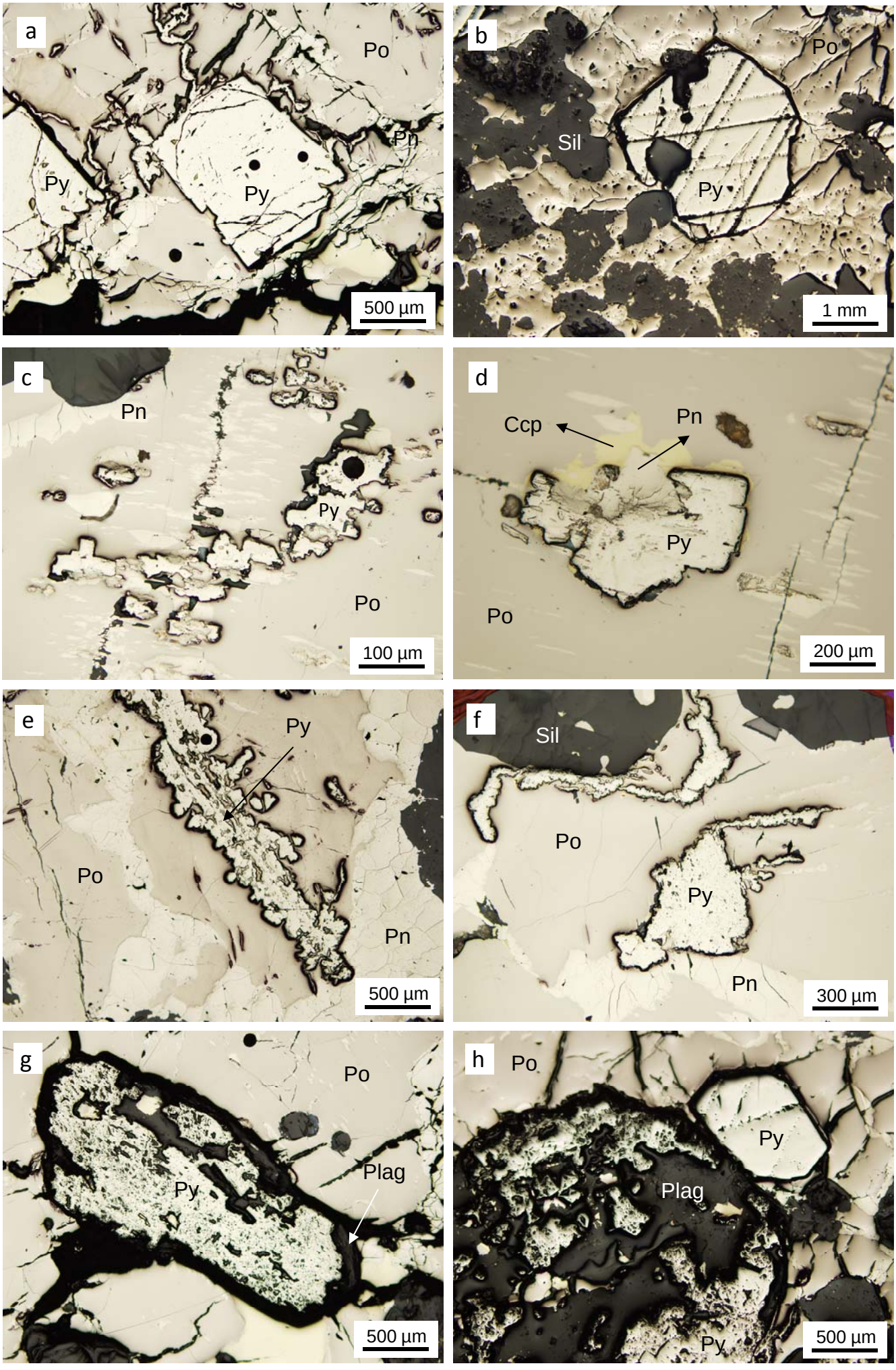
a
Po
Pn
Py
Py
500 µm
b
Po
Sil
Py
1 mm
c
Pn
Py
Po
100 µm
d
Ccp
Pn
Py
Po
200 µm
e
Py
Po
Pn
500 µm
f
Sil
Po
Py
Pn
300 µm
g
Po
Plag
Py
500 µm
h
Po
Py
Plag
Py
500 µm

Figure 2

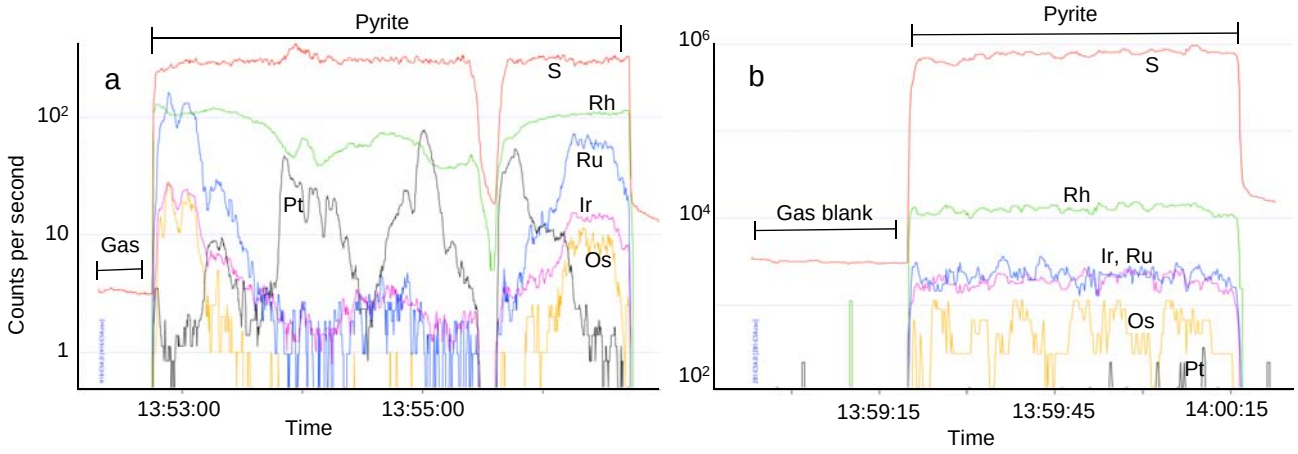
a
Pyrite
S
Rh
Ru
Pt
Ir
Os
Gas
Counts per second
10^2
10
1
13:53:00
13:55:00
Time
b
Pyrite
10^6
10^4
10^2
S
Rh
Gas blank
Ir, Ru
Os
Pt
13:59:15
13:59:45
14:00:15
Time

Figure 3

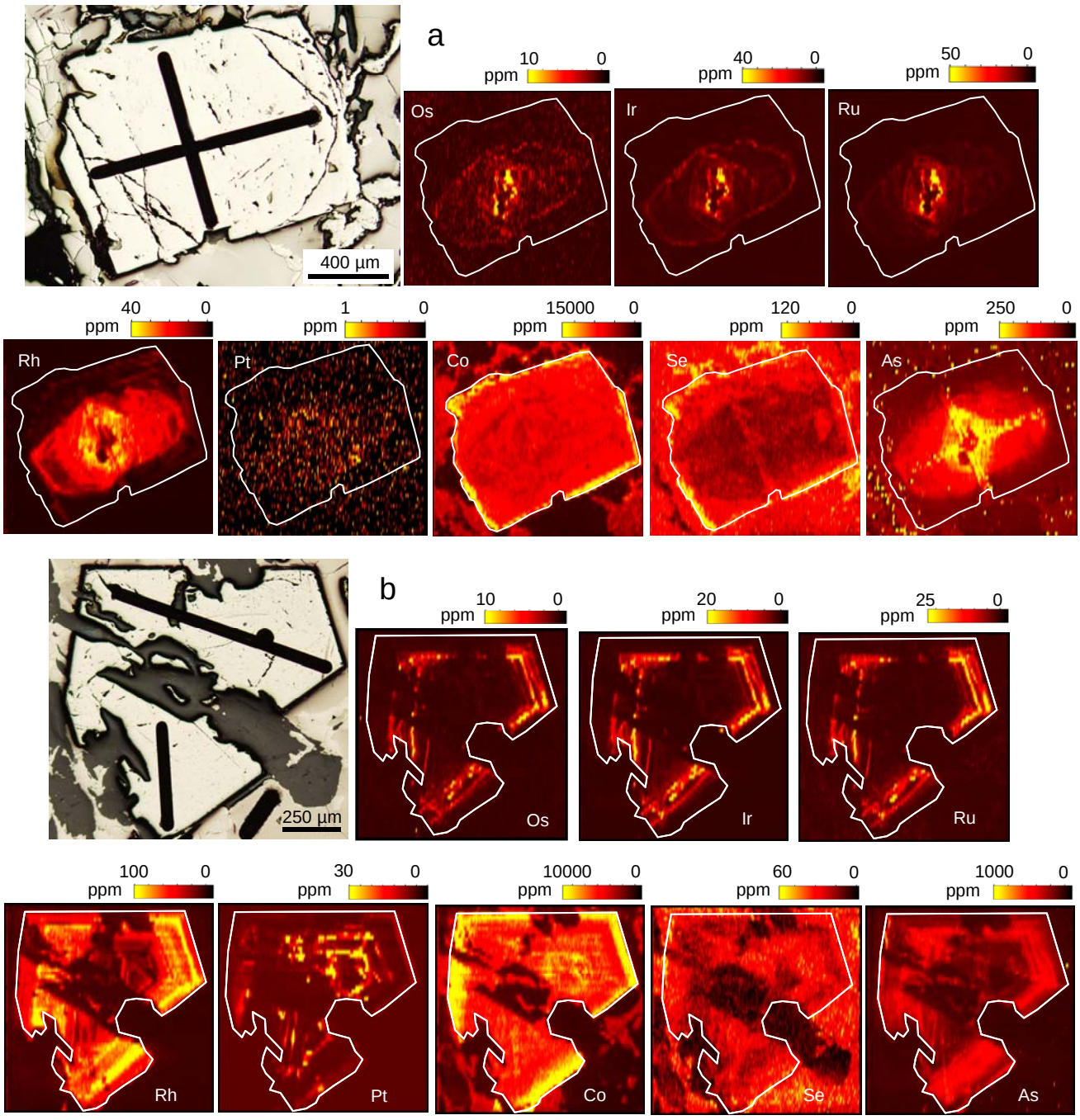
a
400 µm
10
0
ppm
Os
40
0
ppm
Ir
50
0
ppm
Ru
40
0
ppm
Rh
1
0
ppm
Pt
15000
0
ppm
Co
120
0
ppm
Se
250
0
ppm
As
b
250 µm
10
0
ppm
Os
20
0
ppm
Ir
25
0
ppm
Ru
100
0
ppm
Rh
30
0
ppm
Pt
10000
0
ppm
Co
60
0
ppm
Se
1000
0
ppm
As

Figure 4

Figure 5

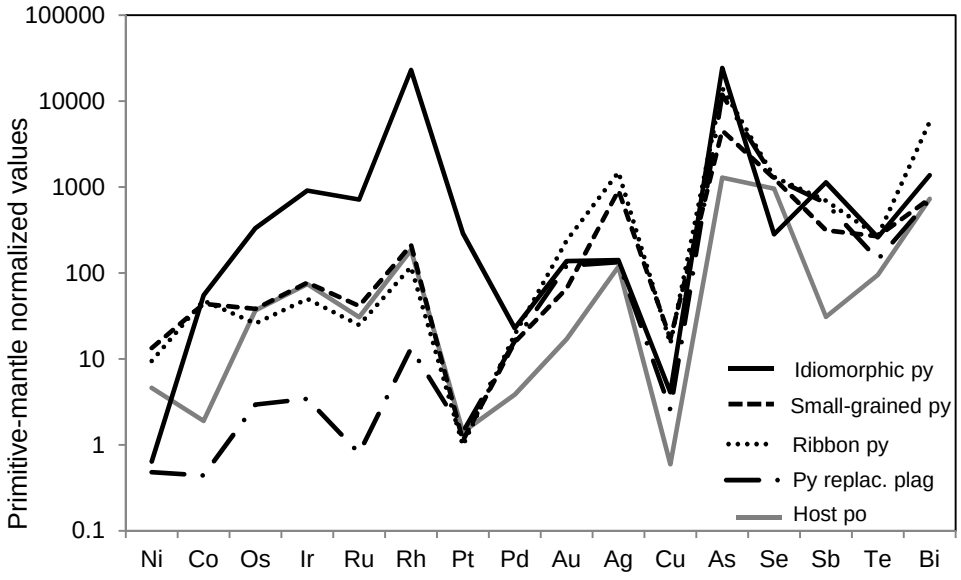
100000
10000
1000
100
10
1
0.1
Primitive-mantle normalized values
Ni
Co
Os
Ir
Ru
Rh
Pt
Pd
Au
Ag
Cu
As
Se
Sb
Te
Bi
Idiomorphic py
Small-grained py
Ribbon py
Py replac. plag
Host po

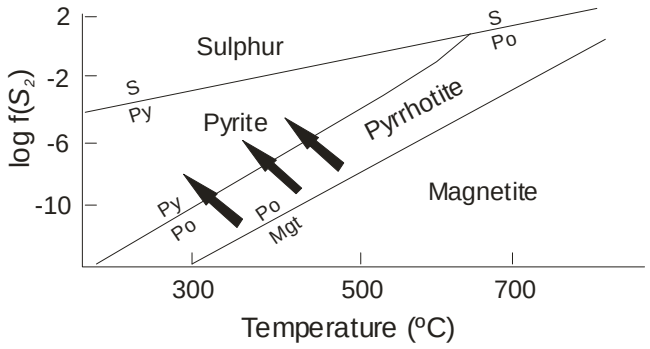
2
-2
-6
-10
log f(S2)
Sulphur
S
Py
S
Po
Pyrite
Pyrrhotite
Magnetite
Py
Po
Po
Mgt
300
500
700
Temperature (ºC)

Figure 6

Figure 7

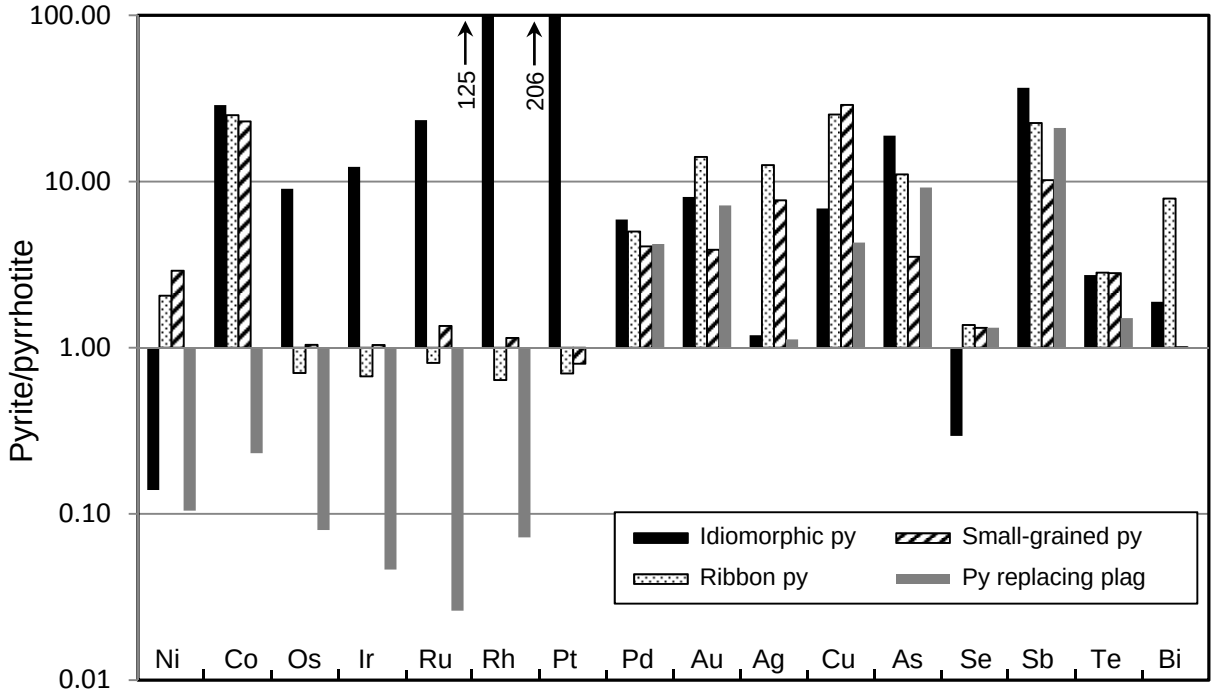
100.00
10.00
1.00
0.10
0.01
Pyrite/pyrrhotite
125
206
Idiomorphic py
Small-grained py
Ribbon py
Py replacing plag
Ni
Co
Os
Ir
Ru
Rh
Pt
Pd
Au
Ag
Cu
As
Se
Sb
Te
Bi

Table 1. Summary of laser ablation ICP-MS results for different types of pyrite and host pyrrhotite from Aguablanca deposit

Element	Co	Ni	Cu	As	Se	Ru	Rh	Pd	Ag	Sb	Te	Os	Ir	Pt	Au	Bi
Isotope	59	61	65	75	82	101	103	105	107	121	125	189	193	195	197	209
Large idiomorphic pyrites (n=5)																
ave	5746	1254	123	1216	21.2	3.578	20.690	0.089	1.13	6.23	3.12	1.129	2.915	2.058	0.137	3.44
stdes	*230*	*266*	*68*	*396*	*3.7*	*2.194*	*8.413*	*0.049*	*0.95*	*4.34*	*1.62*	*1.069*	*2.403*	*3.916*	*0.063*	*3.74*
max	*6030*	*1660*	*197*	1600	25.6	7.108	32.000	0.146	2.50	13.40	5.02	2.860	6.580	9.020	0.234	9.30
min	*5430*	*980*	*44*	560	16.1	1.124	10.210	0.034	0.14	3.00	1.10	0.150	0.465	0.054	0.077	0.45
Ribbon-like pyrites (*n*=13)																
ave	4990	18490	452	711	98.4	0.124	0.106	0.075	11.92	3.83	3.23	0.088	0.160	<0.007	0.239	14.37
stdes	*2154*	*16241*	*320*	*1138*	*12.3*	*0.076*	*0.062*	*0.047*	*4.84*	*2.44*	*2.89*	*0.080*	*0.134*		*0.152*	*16.47*
max	*8140*	*62000*	*1110*	*4100*	*117.9*	*0.268*	*0.238*	*0.180*	*25.63*	*9.80*	*8.70*	*0.277*	*0.469*	*0.022*	*0.500*	*62.20*
min	*1839*	*4036*	*101*	*4.6*	*75.8*	*0.050*	*0.046*	*0.028*	*6.05*	*1.38*	*0.69*	*0.017*	*0.045*	*<0.007*	*0.023*	*2.27*
Small-grained pyrites (n=10)																
ave	4584	26165	517	227	94.6	0.207	0.190	0.061	7.32	1.73	3.20	0.130	0.247	<0.008	0.066	1.83
stdes	*2914*	*14077*	*958*	*261*	*9.9*	*0.035*	*0.032*	*0.048*	*8.42*	*1.40*	*1.18*	*0.030*	*0.047*		*0.060*	*1.27*
max	*9170*	*46000*	*3200*	*750*	*106.1*	*0.275*	*0.218*	*0.161*	*27.40*	*4.60*	*5.16*	*0.183*	*0.313*	*0.010*	*0.185*	*5.21*
min	*1393*	*6490*	*35*	*19*	*80.7*	*0.151*	*0.112*	*0.013*	*0.44*	*0.14*	*1.77*	*0.077*	*0.153*	*<0.008*	*0.018*	*0.87*
Pyrites replacing to plagioclase (n=13)																
ave	46.1	940	76.6	593	94.8	<0.004	0.012	0.063	1.06	3.57	1.72	<0.010	0.011	<0.010	0.122	1.80
stdes	*41.5*	*853*	*55.8*	*647*	*39.8*		*0.009*	*0.043*	*0.68*	*2.59*	*0.89*		*0.013*		*0.116*	*2.15*
max	*126.0*	*2740*	*208.0*	*1730*	*203.0*	*0.031*	*0.026*	*0.167*	*2.27*	*8.40*	*3.45*	*<0.010*	*0.036*	*0.030*	*0.370*	*7.10*
min	*4.9*	*51*	*14.9*	*17*	*52.0*	*<0.004*	*0.001*	*0.016*	*0.24*	*0.42*	*0.73*		*<0.003*	*<0.004*	*0.012*	*0.10*
Host pyrrhotite (n=20)																
ave	204	8751	18.7	67.6	72.2	0.149	0.168	<0.015	0.96	0.17	1.87	0.122	0.232	<0.018	<0.020	1.15
stdes	*90*	*2277*	*20.4*	*75.0*	*4.9*	*0.095*	*0.090*		*0.64*	*0.13*	*1.49*	*0.061*	*0.128*			*0.46*
max	*386*	*13970*	*83.0*	330.0	81.0	0.242	0.286	0.028	2.36	0.61	5.03	0.206	0.374	0.034	0.028	2.23
min	*97.2*	*5710*	*2.0*	1.6	65.2	0.015	0.046	<0.010	0.28	0.06	0.56	0.035	0.055	<0.010	<0.010	0.31

Values in ppm. *n* number of grains analyzed, *ave* average, *stdes* standard deviation, *max* maximum value, *min* minimum value, < below detection limit.

Table S1. Reference materials and values used to calibrate the laser and results for in-house reference materials used as monitor

Isotope		34S %	57Fe %	59Co ppm	61Ni %	65Cu %	75As ppm	82Se ppm	101Ru ppm	103Rh ppm	105Pd ppm	107Ag ppm	121Sb ppm	125Te ppm	189Os ppm	193Ir ppm
Reference materials used for calibration of sulfide minerals																
		po-727	po-727	mass-1	jbmss5	mass-1	mass-1	mass-1	po-727	po-727	po-727	mass-1	mass-1	mass-1	po-727	po-727
	Working values	39	61.1	67	1.05	13.4	65	53	36.3	41.4	43.1	67	55	21	46.9	47.8
	stdev	0.4	0.2	n.d.	n.d.	n.d.	n.d.	n.d.	0.3	0.3	0.4	n.d.	n.d.	0.7	2.5	1.2
	Based on	Certif.	Certif.	W 2002	AA	W 2002	W 2002	W 2002	Certif.	Certif.	Certif.	W 2002	W 2002	Nist610	Certif.	Certif.
Values obtained for in-house reference materials																
UQAC-MSS1, $NiFeS_2$																
	Working values	38.00	30.30	99.00	31.00	0.003	n.d.	5.30	1.75	0.94	1.26	0.27	0.08	0.19	1.90	1.37
	stdev	0.50	1.30	1.00	7.00	0.001		0.35	0.03	0.01	0.05	0.08	0.03	0.06	0.01	0.01
	Based on	EMP	EMP	Nist610	EMP	Nist610		Nist610	ID-sol	ID-sol	ID-sol	Nist610	Nist610	Nist610	ID-sol	ID-sol
This study	average	37.06	Int std	114.09	32.88	0.004		5.53	2.34	0.89	1.10	0.18	0.20	0.23	1.46	1.29
n = 22	stdev	0.69		1.7	11.63	<0.001		0.34	0.07	0.02	0.05	0.03	0.05	0.07	0.08	0.04
	Rel. Diff.	0.98		1.15	1.06	1.27		1.04	1.34	0.95	0.87	0.67	2.50	1.21	0.77	0.94
JBMSS5, FeS																
	Working values	40	57	n.d.		0.021	79.00	48.4	21.70	61.40	64.10	60.70	61.30	44.00	42.60	44.00
	stdev	0.60	0.90			0.001	11.00	14.80	n.d.	7.20	n.d.	3.70	7.30	3.00	0.93	n.d.
	Based on	po727	po727			AA	ICP-sol	Nist610	ID-sol	ICP-sol	ID-sol	ICP-sol	ICP-sol	Nist610	ICP-sol	ID-sol
This study	average	37.94	Int std			0.024	92.35	54.72	21.74	60.33	55.44	61.12	48.61	40.71	60.19	42.63
n = 24	stdev	0.76				0.001	34.99	1.44	0.35	0.77	0.87	1.35	1.13	1.30	1.09	0.65
	Rel. Diff.	0.95				1.14	1.17	1.13	1.00	0.98	0.86	1.01	0.79	0.93	1.41	0.97

Certif.: values certified obtained by solution ICP-MS. W 2002 = Wilson et al. (2002). AA: aqua regia solution followed by atomic absorption. Nist610: laser ablation using Nist610 to calibration. ID-sol: isotope d
aqua regia disolution followed by ICP-MS. EMP = electron microprobe. stdev: standard deviation; n.d.: not determined; int std: internal standard; n number of analyses; Rel. Diff.: relative difference of this stud

195Pt ppm	197Au ppm	209Bi ppm
po-727	po-727	mass-1
35.4	45.8	66
0.8	2.3	0.9
Certif.	Certif.	Nist610
1.66	1.21	<0.02
0.01	0.24	n.d.
ID-sol	Nist610	Nist610
1.30	1.19	0.08
0.07	0.08	0.02
0.78	0.98	
39.30	35.90	76.10
1.00	4.80	2.9
ID-sol	ICP-sol	ICP-sol
39.78	37.24	76.04
0.68	0.80	1.74
1.01	1.04	1.00

dilution followed by ICP-MS. IC
dy/workinç

TABLE S2. Individual laser ablation ICP-MS results for the different textural types of pyrite from Aguablanca

Element	Co	Ni	Cu	Os	Ir	Ru	Rh	Pt	Pd	Au	Ag	As	Sb	Se	Bi	Te
Isotope	59	61	65	189	193	101	103	195	105	197	107	75	121	82	209	125
Large idiomorphic, PGE-rich pyrites																
281-c2a	6030	1660	83	0.150	0.465	1.124	25.870	0.041	0.042	0.167	0.14	1370	13.40	16.1	0.45	2.26
Leo-py4	5804	1350	197	0.630	1.612	3.080	17.190	0.103	0.146	0.234	2.50	1600	7.19	25.6	4.92	4.50
Leo-py6	5614	980	44	0.596	1.970	2.860	10.210	0.054	0.034	0.099	0.47	1180	3.18	23.9	0.55	5.02
416-py1	5430	1200	190	2.860	6.580	7.108	32.000	9.020	0.115	0.077	0.90	1370	3.00	20.6	1.96	1.10
416-py2	5850	1080	100	1.410	3.950	3.718	18.180	1.070	0.106	0.110	1.64	560	4.40	19.7	9.30	2.71
Ribbon-like pyrites																
415-c4a	1839	17580	273	0.018	0.082	0.057	0.058	<0.011	0.058	0.367	25.63	4100	9.80	104.7	8.93	2.67
415-c5a	4690	23830	376	0.028	0.065	0.071	0.046	<0.007	0.029	0.279	12.38	1240	5.70	105.1	12.82	1.37
415-c6a	4910	34600	390	0.017	0.055	0.073	0.046	<0.009	0.071	0.494	11.75	1030	5.50	117.9	29.60	8.63
415-c12a	7690	25260	231	0.038	0.071	0.052	0.052	0.022	0.095	0.358	10.68	1520	3.99	111.8	20.31	5.10
281-c1a	5780	4610	663	0.154	0.276	0.202	0.198	<0.009	0.115	0.177	10.43	310	3.02	98.2	4.53	1.55
281-c3a	3500	9400	1030	0.149	0.302	0.211	0.181	<0.004	0.091	0.189	14.49	270	3.32	91.8	2.97	1.10
416-c2a	4670	20460	173	0.048	0.080	0.056	0.094	0.017	0.045	0.215	9.26	310	2.70	107.2	17.00	8.70
416-c3a	7220	62000	1110	0.037	0.072	0.134	0.110	<0.007	0.180	0.172	7.73	330	1.38	99.8	62.20	2.01
416-c4a	1980	19300	373	0.024	0.069	0.050	0.076	<0.005	0.032	0.500	11.83	82	1.89	95.4	8.18	5.96
AB3-c7a	3250	4036	476	0.176	0.281	0.193	0.238	<0.005	0.134	0.123	12.93	16	3.39	85.6	2.27	0.69
AB16-c1c	3640	9250	128	0.118	0.217	0.172	0.086	<0.007	0.028	0.023	6.05	5	1.38	80.8	2.28	0.94
AB16-c1d	8140	4660	101	0.067	0.045	0.077	0.126	<0.007	0.030	0.064	7.71	11	1.47	75.8	4.84	1.09
AB16-c3a	7560	5380	555	0.277	0.469	0.268	0.073	0.020	0.067	0.148	14.02	15	6.19	105.5	10.89	2.12
Small-grained pyrites																
281-c4a	4220	15820	205	0.164	0.282	0.208	0.185	<0.005	0.048	0.057	10.27	240	1.79	83.9	2.31	5.16
281-c5a	2055	36500	234	0.125	0.266	0.202	0.173	<0.008	0.135	0.185	2.78	750	4.60	86.6	5.21	3.94
281-c6a	7730	44200	630	0.183	0.313	0.275	0.216	<0.006	0.057	0.054	12.43	610	3.08	80.7	1.44	2.30
281-c6b	7070	46000	153	0.138	0.274	0.245	0.190	<0.016	0.033	0.049	27.40	68	2.69	85.0	1.33	2.79
281-c7a	1393	24600	35	0.077	0.153	0.151	0.112	<0.007	0.013	0.021	0.69	340	0.14	95.0	0.87	2.86
AB3-c2a	2750	23240	99	0.113	0.187	0.168	0.174	0.010	0.021	0.033	0.44	48	0.50	104.8	1.18	4.14
AB3-c3a	7210	20700	3200	0.141	0.265	0.203	0.218	<0.010	0.161	0.018	3.50	42	0.58	106.1	1.30	4.62
AB3-c4a	2440	8100	286	0.134	0.253	0.202	0.211	<0.008	0.061	0.045	2.19	53	1.04	103.0	1.95	1.96
AB3-c5a	9170	6490	263	0.116	0.248	0.202	0.207	<0.005	0.043	0.167	11.60	19	2.05	96.1	0.97	2.50
AB3-c9a	1798	36000	62	0.106	0.228	0.211	0.215	<0.004	0.039	0.031	1.88	101	0.84	104.9	1.73	1.77
Pyrites replacing to plagioclase																
415-c2a	63.0	1560	163	<0.011	0.018	0.031	0.022	0.030	0.121	0.370	1.46	1730	8.40	91.5	4.53	2.38
415-c3a	120.0	2740	100	<0.011	0.029	0.013	0.025	0.022	0.167	0.270	2.11	1300	6.90	59.9	7.10	2.94
415-c7a	46.0	1230	93	<0.007	0.014	<0.006	0.026	<0.015	0.092	0.190	1.46	1170	4.59	72.9	3.52	2.78
415-py	126.0	2130	62	<0.010	<0.005	0.012	0.009	<0.007	0.054	0.143	1.06	1110	5.90	54.7	2.31	1.46
415-c8a	22.7	1640	51	<0.018	<0.003	<0.004	<0.002	<0.009	0.019	0.224	0.41	1460	6.70	87.4	0.29	1.78
415-c9a	11.7	710	15	<0.007	<0.005	<0.003	0.005	<0.015	0.016	0.032	0.24	310	1.68	92.1	0.10	0.90
Leo-py2	8.2	488	50	<0.014	<0.003	<0.004	0.003	<0.007	0.038	0.024	2.27	17	1.23	83.3	0.22	1.39
Leo-py3	4.9	51	62	<0.013	<0.004	<0.005	0.004	<0.007	0.046	0.017	1.05	48	2.39	52.0	0.63	1.24
416-c6a	67.0	337	208	<0.024	0.029	<0.004	0.022	0.030	0.084	0.172	1.33	183	2.36	125.6	2.50	3.45
AB8-c2a	8.1	740	27	<0.018	<0.003	<0.007	0.011	<0.017	0.035	0.067	0.28	38	1.90	112.7	0.25	1.46
AB8-c5b	74.0	300	17	<0.030	<0.007	<0.006	0.005	<0.020	0.032	0.016	0.24	200	0.42	203.0	0.39	0.84

AB3-c1a	22.9	126	84	<0.015	<0.007	<0.010	0.009	<0.015	0.061	0.012	0.69	28	1.87	79.9	0.17	0.73
AB3-c10a	25.0	172	65	<0.022	0.036	<0.007	0.016	<0.013	0.055	0.049	1.25	120	2.06	117.5	1.35	0.97

Values in ppm. < below detection limit.

TABLE S3. Individual laser ablation ICP-MS results for pyrrhotites from Aguablanca

Element	Co	Ni	Cu	Os	Ir	Ru	Rh	Pt	Pd	Au	Ag	As	Sb	Se	Bi	Te
Isotope	59	61	65	189	193	101	103	195	105	197	107	75	121	82	209	125
415-C4B	213.0	12250	34.8	0.048	0.081	0.033	0.050	<0.027	0.014	0.020	2.33	86.0	0.28	74.2	0.31	3.35
415-C5B	98.6	10520	10.5	0.057	0.055	0.027	0.046	<.0.023	0.008	<0.019	0.64	63.8	0.61	78.5	0.84	2.56
415-C6B	132.2	11390	5.1	0.036	0.068	0.031	0.063	<0.042	0.009	<0.020	0.48	112.0	0.15	70.8	1.57	3.59
415-C12B	97.2	11350	2.2	0.035	0.075	0.015	0.049	<0.028	0.012	0.028	1.72	330.0	0.06	72.3	1.24	4.08
281-C1C	132.1	6920	6.9	0.155	0.348	0.239	0.220	<0.028	0.015	<0.014	0.43	56.0	0.21	72.4	1.00	0.88
281-C3B	223.3	6830	11.4	0.172	0.322	0.204	0.194	<0.022	<0.010	0.020	0.86	50.6	0.18	72.1	0.79	1.76
416-C2B	251.0	5710	6.6	0.050	0.073	0.049	0.092	<0.018	0.018	<0.010	2.36	52.0	0.31	74.4	1.21	3.74
416-C3B	314.0	5960	83.0	0.055	0.078	0.034	0.108	<0.013	0.026	<0.015	1.37	90.0	0.22	70.0	1.07	5.03
416-C4B	138.7	5840	22.0	0.052	0.081	0.039	0.096	0.034	<0.022	0.022	1.06	34.2	0.07	66.2	0.74	3.86
AB3-C7B	386.0	7290	51.0	0.189	0.338	0.229	0.274	<0.019	<0.021	<0.015	1.01	24.3	0.18	79.2	1.31	0.56
AB16-C1A	102.8	13970	2.0	0.206	0.358	0.228	0.135	<0.001	0.004	<0.003	0.80	1.6	0.07	65.2	0.99	0.75
AB16-C3B	380.0	10550	33.4	0.115	0.138	0.066	0.058	0.009	0.008	<0.005	1.37	1.8	0.18	77.7	0.64	1.21
281-C4B.D	174.5	7540	31.0	0.158	0.322	0.220	0.217	<0.020	<0.010	0.020	0.28	61.0	0.06	68.2	1.20	0.77
281-C5B.D	120.7	7730	4.5	0.160	0.324	0.199	0.206	<0.029	0.028	0.013	0.28	190.0	0.25	65.4	1.94	0.96
281-C6D.D	287.0	8960	11.8	0.122	0.307	0.207	0.216	<0.021	<0.005	<0.012	0.69	37.0	0.05	66.7	1.22	0.88
281-C7B.D	152.6	8710	4.3	0.134	0.294	0.240	0.217	<0.021	0.021	<0.014	0.45	50.3	0.16	67.7	2.23	0.84
AB3-C2B.D	146.6	7850	25.7	0.197	0.344	0.237	0.273	<0.014	<0.017	<0.028	0.38	22.5	0.21	76.4	1.81	0.63
AB3-C4B.D	209.0	7840	18.5	0.154	0.374	0.242	0.278	<0.037	<0.014	<0.033	1.60	18.2	0.07	81.0	1.03	0.70
AB3-C5C.D	234.0	8880	5.1	0.198	0.354	0.214	0.286	<0.013	0.018	<0.025	0.44	33.0	0.09	68.9	0.95	0.65
AB3-C9B.D	285.0	8920	3.4	0.136	0.303	0.218	0.276	<0.014	<0.022	<0.017	0.67	37.0	0.06	76.3	0.82	0.69

Values in ppm. < below detection limit.